ACS OMEGA

http://pubs.acs.org/journal/acsodf

Article

Two Orders of Magnitude Boost in the Detection Limit of Droplet-Based Micro-Magnetofluidics with Planar Hall Effect Sensors

Julian Schütt,* Rico Illing, Oleksii Volkov, Tobias Kosub, Pablo Nicolás Granell, Hariharan Nhalil, Jürgen Fassbender, Lior Klein, Asaf Grosz, and Denys Makarov*

Cite This: *ACS Omega* 2020, 5, 20609−20617

Read Online

ACCESS | Metrics & More | Article Recommendations | Supporting Information

ABSTRACT: Magnetofluidics is a dynamic research field, which requires novel sensor solutions to boost the detection limit of tiny quantities of magnetized objects. Here, we present a sensing strategy relying on planar Hall effect sensors in droplet-based micro-magnetofluidics for the detection of a multiphase liquid flow, i.e., superparamagnetic aqueous droplets in an oil carrier phase. The high resolution of the sensor allows the detection of nanoliter-sized superparamagnetic droplets with a concentration of 0.58 mg/cm^3, even when they are biased in a geomagnetic field only. The limit of detection can be boosted another order of magnitude, reaching 0.04 mg/cm^3 (1.4 million particles in a single 100 nL droplet) when a magnetic field of 5 mT is applied to bias the droplets. With this performance, our sensing platform outperforms the state-of-the-art solutions in droplet-based micro-magnetofluidics by a factor of 100. This allows us to detect ferrofluid droplets in clinically and biologically relevant concentrations and even below without the need of externally applied magnetic fields. These results open the route for new strategies of the utilization of ferrofluids in microfluidic geometries in, e.g., bio(−chemical) or medical applications.

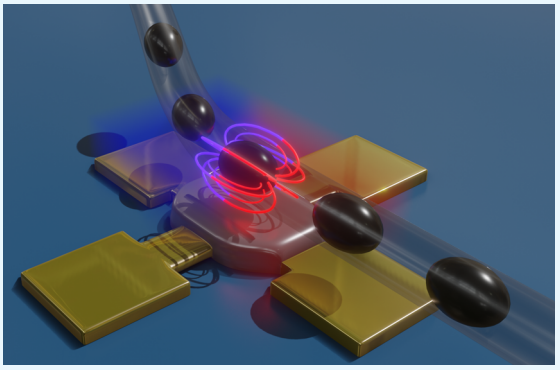

INTRODUCTION

The detection, manipulation, and tracking of magnetic nanoparticles (MNPs) are of major importance for applications in the fields of biology, biotechnology, and biomedicine as labels as well as for drug delivery, (bio)detection, and tissue engineering.[1] Here, a very low background noise due to the lack of any magnetic material in biological samples is provided, and excellent biocompatibility can be found, e.g., for Fe_3O_4 and γ-Fe_2O_3 nanoparticles.[2] Introduced into biological tissues, they show high potential in state-of-the-art medical diagnostics in, e.g., magnetic resonance imaging (MRI)[3,4] as contrast agents and as drug delivery vessels.[5] For applications in MRI, the MNP concentration has to be precisely controlled in the range of less than 1 mg/cm^3.[6−10] One of the main emphases of utilization of MNPs in biological context is in cancer thermotherapy, where the concentration of MNPs (typically[11−17] in the range of mg/cm^3) has to be carefully assigned owing to its severe impact on the heating efficiency. MNPs hold big potential in the research field of biosensorics and point-of-care diagnostics due to their possibility to capture and isolate rare biomarkers and molecules by their high surface-to-volume ratio and magnetic properties.[18] The detection of small quantities or low concentrations of functionalized MNPs, bound to their specific target, allows improvement over the existing state-of-the-art technologies.[19−21] In this respect, ultrasensitive detection of molecules and biomarkers, probed by MNPs, was demonstrated[22,23] down to a single molecule detection level using, e.g., nanopore sensors.[24]

To comply with the stringent requirements of modern research, existing chemical, biological, and medical procedures evolve to become time and cost efficient by enabling a high-throughput analysis of in vitro liquid samples at ultralow volumes. Microfluidics offers vast advantages to address these requirements as it deals with the control and manipulation of liquids in confined channels, usually with a diameter of several micrometers up to millimeters. Additional functionalities can be added to this technology by introducing a second flow of an immiscible liquid by, e.g., flow-focusing and T-junction geometries.[25,26] This transition from a continuous or single-flow fluidics to a multi-flow fluidics (also known as droplet microfluidics) provides major improvement of various medical and (bio)chemical operations and assays. This technology allows to realize homogenized isolated droplets, or micro-environments, allowing high-throughput sample creation at ultralow volumes down to femtoliters[27] as well as high

Received: June 16, 2020
Accepted: July 21, 2020
Published: August 10, 2020

https://dx.doi.org/10.1021/acsomega.0c02892
ACS Omega 2020, 5, 20609−20617

automatization potential by droplet splitting,[28] merging, incubation, and mixing.[29] Using this methodology, various application scenarios were demonstrated, e.g., polymerase chain reaction (PCR),[30] drug screening,[31] immunoassays,[32] electrophoresis,[33] cell sorting,[34] and single cell analysis.[35] In the research field of sensorics, it enables safe liquid sample transport to the sensing structures, minimizing the risks of contamination and further enables additional liquid manipulation. Various strategies are present to detect microfluidic droplets in a continuous stream, e.g., optical methods like bright-field and fluorescence microscopy,[34,36] laser-induced fluorescence,[37] and Raman spectroscopy[38] as well as electrochemical methods using, e.g., field-effect transistors[39] and capacitors.[40]

During the last decades, the combination of magnetism, micro-magnetofluidics, and microfluidics gained major interest due to its potential for novel functionalities in lab-on-a-chip approaches like sensing and actuating.[41,42] In this regard, droplet-based micro-magnetofluidics, also known as continuous-flow micro-magnetofluidics,[41] emerged as a novel analytic tool encompassing integrated novel functionalities, e.g., analytics in a flow cytometry format,[43−45] magnetic barcoding,[46] and sorting of magnetically encoded emulsion droplets.[47,48] Novel high-capacity indexing schemes were put forth based on multiphase microfluidic networks for large-scale screening applications.[47,48] These features are crucial to address the needs of modern medical research, e.g., drug discovery.[49]

For these applications, high-performance magnetic field sensors have to be integrated in microfluidic geometries to enable real-time tracking of low concentrations of magnetic species in droplets as they flow by the sensor. The detection of magnetically active liquids and particles has been demonstrated in both dynamic[50,51] and static fashion[52] down to a resolution of one particle and down to 4 mg/cm^3 for nanoparticle-based ferrofluids in dynamic droplet flow.[44,47] In a continuous flow fluidics, giant magnetoresistance (GMR),[49,53,54] anisotropic magnetoresistance (AMR),[55,56] tunnel magnetoresistance (TMR),[57,58] spin valve,[59,60] and planar Hall effect (PHE)[61] sensors were successfully applied to achieve detection of various (non)biological specimens. However, only a few investigations were carried out toward the integration of magnetoresistive sensors (GMR and spin valves) into droplet-based micro-magnetofluidic platforms,[62−66] missing the opportunities granted by droplet microfluidics like automatization possibilities, lower sample consumption, higher throughput, and higher sensitivity. In this context, further improvements have to be conducted in order to boost the sensitivity toward point-of-care analysis and biological or medical applications by, e.g., utilization of nanosized particles and circumventing the need of magnetic biasing of the paramagnetic species and the sensor itself. Among the broad variety of magnetoresistive sensors, PHE sensors gained high interest based on their superior equivalent magnetic noise of 5 pT/$\sqrt{\text{Hz}}$ at 10 Hz,[67] making them promising candidates for state-of-the-art dynamic (in-flow) magnetic droplet detection systems. Here, we present for the first time the detection and analysis of nanoliter-sized superparamagnetic droplets utilizing the PHE sensor (Figure 1). Droplets encapsulate a ferrofluid composed of 10 nm Fe_3O_4 nanoparticles at concentrations ranging from 0.04 to 5 mg/cm^3, which are relevant for biological and medical applications like cancer thermotherapy and MRI. The sensor was placed outside of a microfluidic tube,

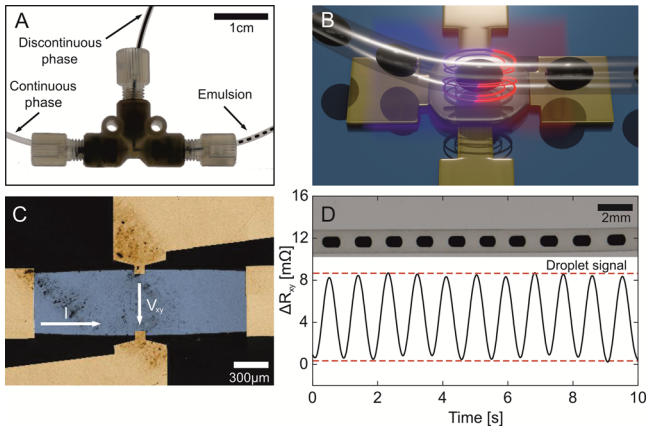

Figure 1. (A) Captured video frame of the microfluidic junction for droplet generation (Video S1). The ferrofluid phase (top, discontinuous phase) is separated into homogeneous nanoliter droplets by the HFE oil phase (continuous phase, left side), accomplished by a T-junction geometry, and guided through the main channel (right side, emulsion phase). (B) Conceptual illustration of the combination of the two technologies, namely, droplet microfluidics (ferrofluid droplets in the HFE oil carrier phase) and PHE-based sensorics. (C) Large-scale SEM image of the PHE sensor center. The change of the in-plane voltage (V_{xy}) is measured perpendicular to the applied current I. (D) Time evolution of the transversal resistance of the PHE sensor (bottom) of passing superparamagnetic droplets (top).

thus avoiding liquid contamination and sensor abrasion even at high flow rates. We examine the sensor response to moving superparamagnetic droplets even without external biasing just in the geomagnetic field and demonstrate the detection of droplets at concentrations down to 0.58 mg/cm^3. With this performance, our detection platform with geomagnetic field biasing droplets with a field of 50 μT outperforms the state-of-the-art devices by 10 times in droplet-based micro-magnetofluidics with integrated GMR sensors yet biased to 1 mT fields.[44] The detection limit of our platform can be pushed down to 0.04 mg/cm^3 when biased with an external magnetic field of 5 mT, which constitutes two orders of magnitude enhancement over the state-of-the-art in droplet-based micro-magnetofluidics. This technology holds great promise for lowering the detection limit of lab-on-a-chip devices relying on the detection of tiny quantities of MNPs and can complement the optical detection methodologies of ferrofluid analysis since all measured concentrations were not distinguishable using conventional optical density (OD) measurements.

RESULTS AND DISCUSSIONS

Setup. Microfluidic ferrofluid droplets in hydrofluoroether (HFE) oil were created in T-junction geometry using a pressure-driven pump in commercial fluorinated ethylene propylene (FEP) tubing with an inner diameter of 500 μm (Figure 1A and Video S1). The volume of individual droplets was varied between 70 and 250 nL by adjusting the flow ratio of the two liquids. Various concentrations of ferrofluid per droplet were achieved by dilution of the stock solution with deionized water. Subsequently, the tube containing ferrofluid droplets was aligned over the PHE sensor (Figure 1B,C), which is a 200 nm-thick permalloy film patterned as an ellipse (long axis along the current flow is 5 mm; short axis along the voltage measurement electrodes is 0.625 mm). The sensor equivalent magnetic noise is better than 200 pT/$\sqrt{\text{Hz}}$ at 1 Hz

https://dx.doi.org/10.1021/acsomega.0c02892
ACS Omega 2020, 5, 20609−20617

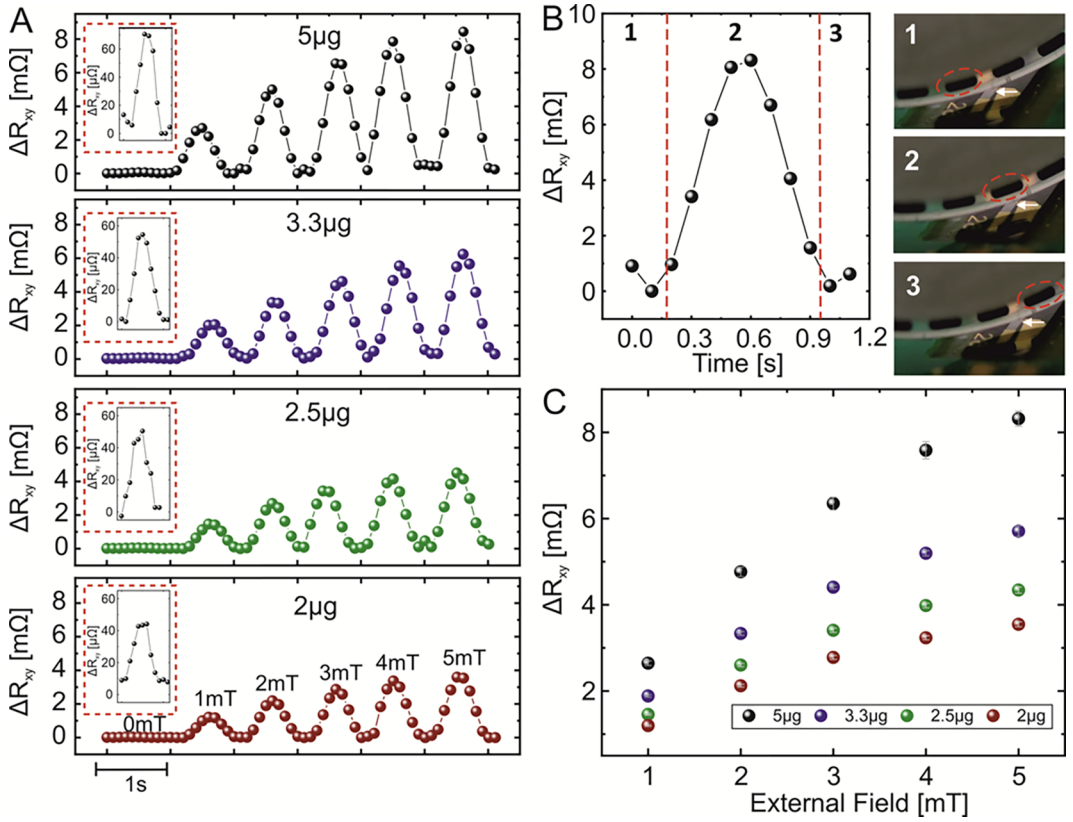

Figure 2. (A) Composite plot showing the sensor readout for a single representative droplet (volume of 100 nL) possessing different concentrations of ferrofluid (weight is indicated in each subpanel) biased to different magnetic fields. The data for each droplet is taken from a measured sequence shown in Figure S4. Insets show zoomed views of the sensor response when droplets are biased to the geomagnetic field. (B) Close-up of the time evolution of the sensor response during the event when a single droplet (5 μg; 5 mT bias) passes above the sensing area. Insets show selected frames of a video sequence (Video S1) at the instances when the droplet (B-1) approaches the sensor, (B-2) is above the sensor, and (B-3) departs from the sensor location. (C) Summary of the maximum sensor responses measured for droplets containing different concentrations of ferrofluid and biased to various magnetic fields.

and above (details are in Figures S1−S3), which increases about 2.5 times when measured in a fluidic setup. The sensor response is quantified as a change of the transversal resistance, R_{xy}, measured at a 60 mA driving current.

The sensing area of the PHE sensor is between the voltage leads, which are 0.625 mm apart (Figure 1C, details are in the Experimental Section and Figure S1). The distance from the sensor to the bottom of the droplet is 550 μm. To improve the sensing performance, we adjust the characteristic diameter of a fluidic droplet to be about 500 μm to match the sensing area of the sensor. To bias ferrofluid droplets to an external magnetic field of up to 5 mT, a dual Helmholtz coil setup was used, and the magnetic field was applied perpendicular to the sensor plane. Figure 1D shows a typical time trace of the PHE sensor readout while a droplet chain (concentration of 5 mg/cm^3 corresponding to 185 million particles per droplet; biasing field of 5 mT) was passing above the sensor. The sensor readout is modified by the in-plane component of the magnetic stray field stemming from each magnetic droplet.

Droplet Detection Using PHE Sensors. Magnetic droplets were biased using an external magnetic field generated by a set of Helmholtz coils. The field varied from 0 to 5 mT. When no field was applied by the coils, the droplets were magnetized by the geomagnetic field. For our geographical location (Dresden, Germany), the magnitude of the magnetic field is close to 50 μT, and the field lines are inclined 66° with respect to the surface. This field can partly align nanoparticles in the droplet along the field lines, leading to a small stray field emanating from the droplet. The PHE sensor response was measured for droplet chains containing various concentrations of a ferrofluid solution. The initial weight of ferromagnetic nanoparticles per droplet with a volume of 100 nL was chosen to be at 5 μg, corresponding to 1.85×10^8 particles per nanoliter or 0.05 μg/nL or 5 mg/cm^3. Further dilutions of the solution led to 3.3, 2.5, and 2 μg of nanoparticle content, or 1.21×10^8, 9.26×10^7, and 7.3×10^7 particles per nanoliter, respectively. These concentrations were chosen due to their relevance for biomedical applications.[6,11,12] The performance of the PHE sensor for the detection of ferrofluid droplets with different concentrations of ferrofluid exposed to different magnetic fields applied perpendicular to the sensor plane is shown in Figure 2A. The droplets flow at a constant speed of 1 mL/h at a flow ratio of ferrofluid-to-oil phases of 1. The entire set of the collected experimental data is summarized in Figure S4, demonstrating the actual transversal resistance readout when droplets are biased to a specific field (5 mT−50 μT geomagnetic field/zero external field). For instance, for a given magnetic content of 5 μg per droplet and a volume of the droplet of 100 nL, the sensor readout is about 40 mΩ in zero external field and 90 mΩ at 5 mT. The sensor response is enhanced with both the increase in the strength of the biasing field and larger concentration of the ferrofluid solution per droplet. Figure 2B depicts a close-up of the sensor response when a single 250 nL droplet (indicated with red circles in the

https://dx.doi.org/10.1021/acsomega.0c02892
ACS Omega 2020, 5, 20609−20617

insets in Figure 2B) is passing over the sensing area (indicated with white arrows in the insets in Figure 2B).

The flow ratio of ferrofluid to oil is 2:1 at a speed of 0.5 mL/h for each flow (Supplementary Video S2). The mass of nanoparticles in the droplet is 5 μg, and the droplet is biased by an external magnetic field of 5 mT. The evolution of the sensor response is correlated with the position of the droplet with respect to the sensor location. A comparison of the maximum PHE sensor response (peak values of the data shown in Figure 2A) for the detection of droplets with various concentrations and biased to different external fields is summarized in Figure 2C (further details are in the Experimental Section). A linear increase in the PHE signal is observed with the increase in the external field for each of the concentration of ferrofluid in droplets. Finally, in contrast to previous measurements, the dynamic change of the magnetic content in droplets was measured in the geomagnetic field in order to evaluate the sensor platform's performance for fast alterations of nanoparticle contents (Figure S5). The discrimination of the signal level is set between 5 and 1 mg/cm^3, similar to the reference measurements discussed above with a sensor resolution of 0.12 (2σ) and 0.24 mg/cm^3 (4σ).

Exploring the Detection Limits. We observe a pronounced sensor response even without application of an external magnetic field using Helmholtz coils (Figure 2A, red boxes), with a sensor response of about 40 $\mu\Omega$ for the smallest nanoparticle mass per droplet (2 μg). This offers an appealing possibility to use our detection platform for tracking biologically and medically relevant ferrofluid concentrations without the use of bulky coils or permanent magnets. In this section, we analyze the limit of detection of our sensing platform when 100 nL of droplets containing different concentrations of ferrofluid are biased to the geomagnetic field and to 5 mT (Figure 3). Each data point represents the mean and standard deviation of the PHE sensor readout measured for 50 droplets. Figure 3 demonstrates the successful detection of the droplets containing down to 0.58 μg of nanoparticles corresponding to the concentration of 0.58 mg/cm^3 or 2.1 × 10^7 particles per nanoliter (top x-axis). If the absolute number of nanoparticles is further reduced, to, e.g., 1.5 × 10^7 (0.4 mg/cm^3), no signal response could be observed in the time domain. Still, a clear response of the sensor is observed if the time-dependent data is transformed into the frequency domain by Fourier transformation (Figure S6). When droplets are biased with 5 mT, even smaller dilutions down to 40 ng (0.04 mg/cm^3) of nanoparticles per droplet are detected, leading to a minimum number of nanoparticles per droplet of about 1.4 millions. In this respect, the detection limit of our sensing platform is by a factor of 100 enhanced compared to the state-of-the-art devices for droplet-based micro-magnetofluidics.[44] We found the detection limit in 5 mT fields via extrapolation of the signal trend at around 5 ng (concentration of 5 μg/cm^3). We account the difference of the measured and theoretical detection limit by the distance of the sensor to the droplets as well as the alignment of the PHE sensor in the external magnetic field.

Sensing Performance for Different Flow Rates and Droplet Sizes in the Geomagnetic Field. In practical settings, it is required to perform measurements under different flow rates and of chains of droplets of different sizes. The result of this characterization is summarized in this section for the case when the droplets are exposed to the geomagnetic field only. First, we fix the ferrofluid-to-oil flow ratio to 1:1, which allows us to produce droplets with a volume of 100 nL. Then, the total flow rate is increased from 1 mL/h (0.5 mL/h for each liquid phase) up to a total flow rate of 20 mL/h. This corresponds to the droplets passing the sensor at a frequency of 0.3 Hz (flow rate of 1 mL/h) up to 13 Hz (flow rate 20 mL/h). The analysis is shown in Figure 4A. Until a droplet frequency of 2.2 Hz (flow rate of 4 mL/h), the peaks can be analyzed based on the time domain data (Figure S7). Further increase in the droplet frequency up to 13 Hz had to be tracked in the frequency domain. Higher droplet frequencies lead to a widening of the frequency-dependent signal and therefore a decrease in the droplet response peak, i.e., from 70 $\mu\Omega$ for 1 mL/h to 10 $\mu\Omega$ for 20 mL/h. We account the difference of signal peak levels to inhomogeneities during the droplet generation. Next, the influence of the droplet size on the sensor response was investigated by keeping the total flow rate constant at 1 mL/h (Figure 4B). To produce droplets of different sizes, the ferrofluid-to-oil flow ratio was changed (1:1, 2:1, and 1:2) resulting in droplet volumes of 100, 250, and 70 nL (insets in Figure 4B), respectively. For all droplet volumes, the signal magnitude stays constant at about 120 $\mu\Omega$. With the increase in the droplet volume, the half width of the peak increases, which is in line with the longer time the droplet spends above the sensor. This assumption is supported by a calculation of the spatial distribution of magnetic stray fields stemming from 70, 100, to 250 nL droplets magnetized in a geomagnetic field (Figure 4C). In these calculations, we treat a droplet as a cylinder with rounded edges of a fixed diameter of 500 μm (details in the Experimental Section). Further, we calculated the stray field for each droplet volume for a pair of droplets in order to see the interaction of the individual stray fields of each droplet in

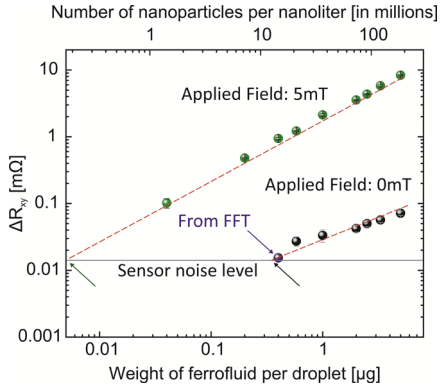

Figure 3. Sensor response while measuring 100 nL droplets containing ferrofluid at different concentrations when the droplets are biased in the geomagnetic field (black points) and biased to 5 mT using Helmholtz coils (green points). In the geomagnetic field, relying on the analysis of the signal in time domain, the limit of detection corresponds to 0.58 μg of nanoparticles per droplet. Fourier transformation of the time-dependent signal allowed detection of droplets containing an even lower concentration of nanoparticles down to 0.4 μg (blue arrow and Figure S6). Utilizing a field of 5 mT using Helmholtz coils, the detection limit is improved by an order of magnitude. Droplets containing 40 ng of magnetic nanoparticles per droplet can be readily detected. The extrapolated theoretical detection limit is located at 0.25 μg in the geomagnetic field (black arrow) and 5 ng in the 5 mT magnetic field (green arrow). The red dashed lines are guides for the eye, and each shown data point is an average of over 50 droplets.

https://dx.doi.org/10.1021/acsomega.0c02892
ACS Omega 2020, 5, 20609−20617

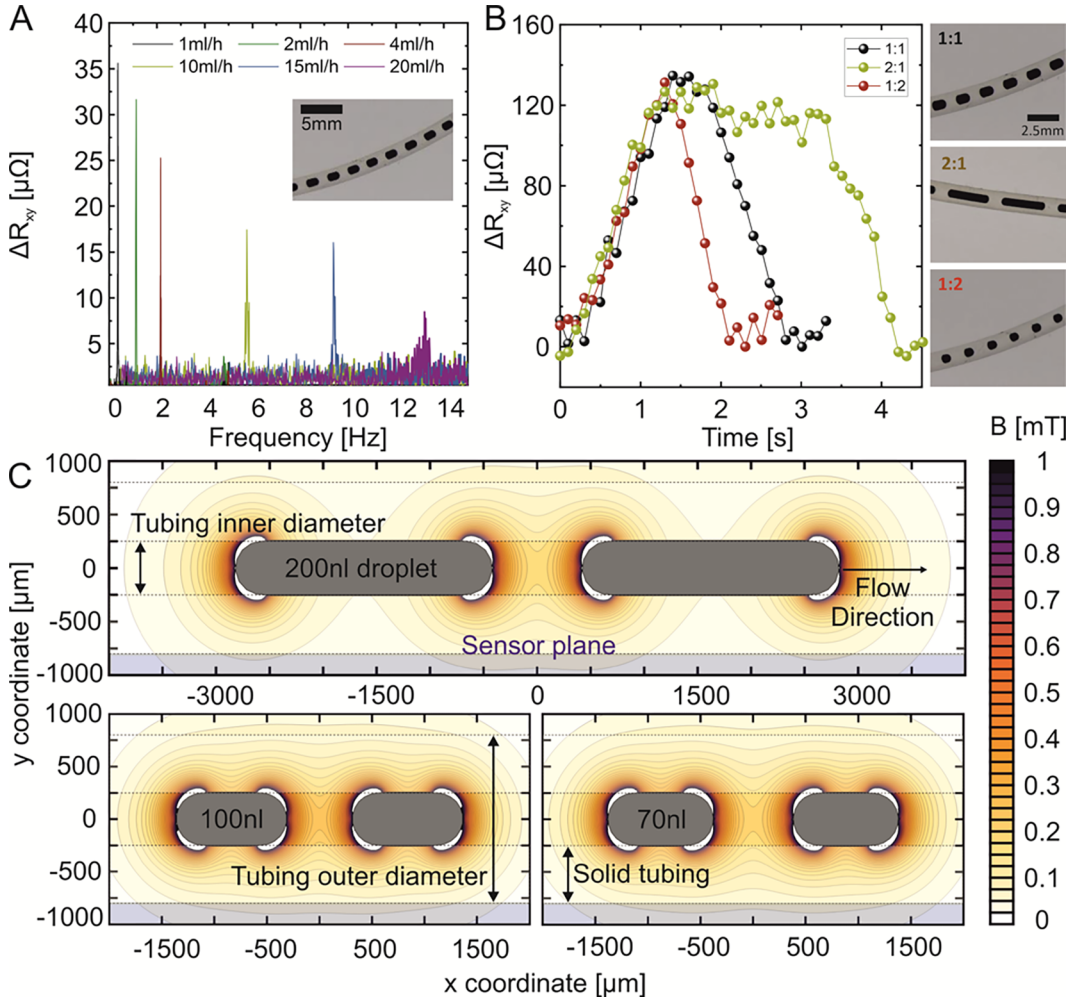

Figure 4. (A) Fourier transformation of the time-dependent PHE readout signal taken from 100 nL droplet sequences prepared at the same flow ratio of ferrofluid to oil of 1:1 and varied flow rate from 1 to 20 mL/h. (B) Close-up of the response signal appearance of one droplet for different droplet volumes. (C) Stray field calculation of two droplets with the volume of 70 and 100 nL. The droplets are biased in the geomagnetic field.

the separating oil phase between them. The calculated stray field of all droplet volumes demonstrated the same magnetic field strength (Figure 4C), explaining the same signal magnitude for various droplet sizes (Figure 4B). However, the spatial extension of stray fields along the motion direction (along the tube) increases for larger droplets, explaining the increased half width of the peak signal for bigger droplet volumes. The most crucial parameter for a correct detection is the distance between the sensor and droplets. The strength of the stray field decays rather fast, therefore it is of advantage to bring the sensor as close as possible to droplets. The orientation of the millifluidic tube plays a minor part as long as the tube passes the sensing area of the sensor, i.e., the area between the measurement electrodes.

CONCLUSIONS

In summary, we present a droplet-based micro-magnetofluidics platform with planar Hall effect sensorics. This combination allows probing of moving superparamagnetic droplets in tubings at various speeds, sizes, and concentrations of magnetically active nanoparticles in the droplets. Utilizing only the geomagnetic field, optically nondifferentiable droplets with the concentration of ferrofluid down to 0.58 mg/cm^3 could be detected, which is relevant for biological and clinical settings. Furthermore, we boost the sensitivity by a factor of 10 in the geomagnetic field (down to 0.4 mg/cm^3) and the state-of-the-art sensitivity by a factor of 100 by using magnetic fields up to 5 mT, thereby complementing the optical detection methodologies of ferrofluid analysis. Doing so, even small changes in the composition or amount of magnetic species in microfluidic droplets become trackable, without being in direct contact with the liquid and thus show a very low chance of contamination the liquid sample. We are convinced that the contactless tracking, probing, and observation of microfluidic droplets can greatly contribute to the state-of-the-art magneto-resistive sensing in the fields of (bio)chemistry, biology, or medical application with dramatic downscaling of the analyzed volume. Further improvement of this conjunction and lower detection limits include optimization of the connecting electronic devices and shielding geometries. Furthermore, utilization of PHE sensors on flexible substrates[68] can greatly improve the system sensitivity since the sensing structures can be brought in very close contact to the rounded tubing.[69] Additionally, the use of nanoparticles with larger magnetization can lead to further improvement in the limit of detection since they will be better aligned in the same magnetic field compared to ferrofluids used in this work. In turn, this will lead to the enhancement of the stray field, which improves the limit of

https://dx.doi.org/10.1021/acsomega.0c02892
ACS Omega 2020, 5, 20609−20617

detection with respect to the amount of magnetic material per droplet. However, care will need to be taken so that these particles do not agglomerate and do not create clusters. Finally, the high sensitivity of the developed platform shows high potential to boost early detection of cancer by functionalization of early cancer markers or antibodies utilizing, e.g., nanoporous iron oxide nanocubes.[70]

EXPERIMENTAL SECTION

Fabrication and Characterization of PHE Sensors. Al_2O_3(60 nm)/Ta(5 nm)/permalloy(200 nm)/Ta(5 nm) films are sputtered on (100)-oriented Si wafers in an ion beam-sputtering (IBS) system (Nanoquest I, Intlvac). A photo-lithography process is used for patterning the extended film into an ellipse with the dimensions of 5 mm in length and 0.625 mm in width (Figure S1). Gold electrical contacts with a thickness of 300 nm are deposited and patterned using a lift-off strategy.[71] Detailed magnetic and electronic noise characterizations were performed on the fabricated PHE sensors (Figures S2 and S3).

Droplet Fabrication and Delivery. Microfluidic droplets were created using T-junctions connected to FEP-based tubings with an inner diameter of 500 μm and outer diameter of 1.6 mm (Dolomite Microfluidics, United Kingdom). While HFE oil was utilized as the permanent phase, aqueous ferrofluid was used as the droplet phase (Supplementary Video S1). The respective liquids are pushed through the tubing by syringes (VWR International, Germany) using a syringe-based pump (nemeSYS 290 N, cetoni GmbH, Germany). Typical flow rates were chosen between 0.5 and 2 mL/h. For high flow rate experiments, the flow rate was increased up to 20 mL/h. The droplet-containing tubing was aligned over the PHE sensor using an adapter guiding the tubing in a semicircle over the sensor region (Supplementary Video S2). Furthermore, the tubing was mechanically thinned at the region where it touched the sensor surface to reduce the distance between droplets and the sensor. Prior to every liquid exchange in the syringes, they were carefully cleaned using acetone, isopropanol, and DI water. Initially, ferrofluid stock solution based on ferromagnetic nanoparticles (EMG700, Ferrotec, USA) was diluted with DI water in a ratio of 1:4. EMG700 contains colloidal nanoparticles with a diameter of about 10 nm, designed in a way to avoid any cluster formation using an anionic surfactant. Assuming a droplet size of 100 nL, each droplet contained 25 nL of the ferrofluid solution or 5 μg of pure nanoparticle mass. Smaller amounts of nanoparticle mass for each droplet were achieved by further dilution of the stock solution.

Data Capture and Analysis. PHE sensors were connected to a resistance tensormeter,[72−75] allowing a direct four-probe measurement with direct data readout. Transverse resistance of the PHE sensor was collected at a drive voltage amplitude of 15 V, resulting in a current amplitude of 60 mA through the sensor, connected in series with a resistor of about 200 ohms. For tests at low particle concentrations, the planar Hall voltage generated by the sensor was stepped 20× using a transformer.

Stray Field Calculations. We calculate the spatial distribution of a magnetic field outside the droplet filled with magnetic nanoparticles. Due to the small size of magnetic nanoparticles and their random distribution inside droplets, we assume that (i) the droplet is homogeneously filled with nanoparticles and (ii) that it could be represented as a magnet of the appropriate shape and dimensions. We numerically calculate the spatial distribution of the magnetic field generated by a droplet considering that the droplet is homogeneously magnetized along the motion direction with a saturation magnetization scaled accordingly to the particle concentration and magnetic moment alignment.

ASSOCIATED CONTENT

Supporting Information

The Supporting Information is available free of charge at https://pubs.acs.org/doi/10.1021/acsomega.0c02892.

Hall effect sensor geometry, resistance and magnetic noise measurements, whole experimental data set for magnetic field gradient, ferrofluid gradient experiment, detection limit in geomagnetic field, droplet speed analysis in the time domain, microfluidic droplet generation, and experimental setup (PDF)

Microfluidic junction for droplet generation (MPG)

Close-up of the experimental setup of the integration of microfluidics and PHE sensorics (MPG)

AUTHOR INFORMATION

Corresponding Authors

Julian Schütt − *Helmholtz-Zentrum Dresden-Rossendorf e.V., Institute of Ion Beam Physics and Materials Research, 01328 Dresden, Germany*; Email: j.schuett@hzdr.de

Denys Makarov − *Helmholtz-Zentrum Dresden-Rossendorf e.V., Institute of Ion Beam Physics and Materials Research, 01328 Dresden, Germany*; Email: d.makarov@hzdr.de

Authors

Rico Illing − *Helmholtz-Zentrum Dresden-Rossendorf e.V., Institute of Ion Beam Physics and Materials Research, 01328 Dresden, Germany*

Oleksii Volkov − *Helmholtz-Zentrum Dresden-Rossendorf e.V., Institute of Ion Beam Physics and Materials Research, 01328 Dresden, Germany*

Tobias Kosub − *Helmholtz-Zentrum Dresden-Rossendorf e.V., Institute of Ion Beam Physics and Materials Research, 01328 Dresden, Germany*

Pablo Nicolás Granell − *Helmholtz-Zentrum Dresden-Rossendorf e.V., Institute of Ion Beam Physics and Materials Research, 01328 Dresden, Germany; Escuela de Ciencia y Tecnología, UNSAM, B1650KNA Buenos Aires, Argentina; Instituto Nacional de Tecnología Industrial, B1650KNA Buenos Aires, Argentina*

Hariharan Nhalil − *Department of Physics & Institute of Nanotechnology and Advanced Materials, Bar-Ilan University, Ramat Gan 5290002, Israel*

Jürgen Fassbender − *Helmholtz-Zentrum Dresden-Rossendorf e.V., Institute of Ion Beam Physics and Materials Research, 01328 Dresden, Germany*

Lior Klein − *Department of Physics & Institute of Nanotechnology and Advanced Materials, Bar-Ilan University, Ramat Gan 5290002, Israel*

Asaf Grosz − *Department of Electrical and Computer Engineering, Ben-Gurion University of the Negev, Beersheba 84105, Israel*

Complete contact information is available at: https://pubs.acs.org/10.1021/acsomega.0c02892

https://dx.doi.org/10.1021/acsomega.0c02892
ACS Omega 2020, 5, 20609−20617

Author Contributions

J.S. and R.I conducted fluidic experiments. L.K., H.N., and A.G. fabricated and optimized the PHE sensors. Simulations were performed by O.V. J.S, D.M, J.F., A.G., and L.K wrote the proposals and oversaw the research in their groups. The data was analyzed by J.S., R.I., and D.M. with contributions from T.K., P.G., and L.K. The manuscript was written by J.S and D.M with inputs from L.K, J.F., T.K, P.G., R.I., and O.V.

Notes

The authors declare no competing financial interest.

■ ACKNOWLEDGMENTS

This work was supported in part by the German Research Foundation (grants MA5144/9-1 and MA5144/14-1), Federal Ministry for Economic Affairs and Energy (BMWi) – WIPANO (FKZ: 03THW12K10), and Helmholtz Association of German Research Centres in the frame of the Helmholtz Innovation Lab "FlexiSens".

■ REFERENCES

(1) Salata, O. Applications of Nanoparticles in Biology and Medicine. *J. Nanobiotechnol.* **2004**, *2*, 3.

(2) Andrä, W.; Häfeli, U.; Hergt, R.; Misri, R. Application of Magnetic Particles in Medicine and Biology. In *Handbook of Magnetism and Advanced Magnetic Materials*; Kronmüller, H., Parkin, S., Eds.; John Wiley & Sons, Ltd: Chichester, UK, 2007; p hmm431.

(3) Berry, C. C.; Curtis, A. S. G. Functionalisation of Magnetic Nanoparticles for Applications in Biomedicine. *J. Phys. D: Appl. Phys.* **2003**, *36*, R198–R206.

(4) Colombo, M.; Carregal-Romero, S.; Casula, M. F.; Gutiérrez, L.; Morales, M. P.; Böhm, I. B.; Heverhagen, J. T.; Prosperi, D.; Parak, W. J. Biological Applications of Magnetic Nanoparticles. *Chem. Soc. Rev.* **2012**, *41*, 4306.

(5) McBain, S. C.; Yiu, H. H. P.; Dobson, J. Magnetic Nanoparticles for Gene and Drug Delivery. *Int. J. Nanomed.* **2008**, *3*, 169–180.

(6) Bevacqua, M. T.; Scapaticci, R. A Compressive Sensing Approach for 3D Breast Cancer Microwave Imaging With Magnetic Nanoparticles as Contrast Agent. *IEEE Trans. Med. Imaging* **2016**, *35*, 665–673.

(7) Pouw, J. J.; Grootendorst, M. R.; Bezooijen, R.; Klazen, C. A. H.; De Bruin, W. I.; Klaase, J. M.; Hall-Craggs, M. A.; Douek, M.; ten Haken, B. Pre-Operative Sentinel Lymph Node Localization in Breast Cancer with Superparamagnetic Iron Oxide MRI: The SentiMAG Multicentre Trial Imaging Subprotocol. *Br. J. Radiol.* **2015**, *88*, 20150634.

(8) Harisinghani, M. G.; Barentsz, J.; Hahn, P. F.; Deserno, W. M.; Tabatabaei, S.; van de Kaa, C. H.; de la Rosette, J.; Weissleder, R. Noninvasive Detection of Clinically Occult Lymph-Node Metastases in Prostate Cancer. *N. Engl. J. Med.* **2003**, *348*, 2491–2499.

(9) Fortuin, A. S.; Brüggemann, R.; van der Linden, J.; Panfilov, I.; Israël, B.; Scheenen, T. W. J.; Barentsz, J. O. Ultra-Small Superparamagnetic Iron Oxides for Metastatic Lymph Node Detection: Back on the Block: USPIOs for Metastatic Lymph Node Detection. *Wiley Interdiscip. Rev.: Nanomed. Nanobiotechnol.* **2018**, *10*, No. e1471.

(10) Yin, X.; Russek, S. E.; Zabow, G.; Sun, F.; Mohapatra, J.; Keenan, K. E.; Boss, M. A.; Zeng, H.; Liu, J. P.; Viert, A.; Liou, S.-H.; Moreland, J. Large T1 Contrast Enhancement Using Superparamagnetic Nanoparticles in Ultra-Low Field MRI. *Sci. Rep.* **2018**, *8*, 11863.

(11) Shah, R. R.; Davis, T. P.; Glover, A. L.; Nikles, D. E.; Brazel, C. S. Impact of Magnetic Field Parameters and Iron Oxide Nanoparticle Properties on Heat Generation for Use in Magnetic Hyperthermia. *J. Magn. Magn. Mater.* **2015**, *387*, 96–106.

(12) de la Presa, P.; Luengo, Y.; Multigner, M.; Costo, R.; Morales, M. P.; Rivero, G.; Hernando, A. Study of Heating Efficiency as a Function of Concentration, Size, and Applied Field in γ-Fe_2O_3 Nanoparticles. *J. Phys. Chem. C* **2012**, *116*, 25602–25610.

(13) Andrés Vergés, M.; Costo, R.; Roca, A. G.; Marco, J. F.; Goya, G. F.; Serna, C. J.; Morales, M. P. Uniform and Water Stable Magnetite Nanoparticles with Diameters around the Monodomain–Multidomain Limit. *J. Phys. D: Appl. Phys.* **2008**, *41*, 134003.

(14) Kang, T.; Li, F.; Baik, S.; Shao, W.; Ling, D.; Hyeon, T. Surface Design of Magnetic Nanoparticles for Stimuli-Responsive Cancer Imaging and Therapy. *Biomaterials* **2017**, *136*, 98–114.

(15) Vegerhof, A.; Motei, M.; Rudinzky, A.; Malka, D.; Popovtzer, R.; Zalevsky, Z. Thermal Therapy with Magnetic Nanoparticles for Cell Destruction. *Biomed. Opt. Express* **2016**, *7*, 4581.

(16) Tay, Z. W.; Chandrasekharan, P.; Chiu-Lam, A.; Hensley, D. W.; Dhavalikar, R.; Zhou, X. Y.; Yu, E. Y.; Goodwill, P. W.; Zheng, B.; Rinaldi, C.; Conolly, S. M. Magnetic Particle Imaging-Guided Heating *in Vivo* Using Gradient Fields for Arbitrary Localization of Magnetic Hyperthermia Therapy. *ACS Nano* **2018**, *12*, 3699–3713.

(17) Wust, P.; Gneveckow, U.; Wust, P.; Gneveckow, U.; Johannsen, M.; Böhmer, D.; Henkel, T.; Kahmann, F.; Sehouli, J.; Felix, R.; Ricke, J.; Jordan, A. Magnetic Nanoparticles for Interstitial Thermotherapy – Feasibility, Tolerance and Achieved Temperatures. *Int. J. Hyperthermia* **2006**, *22*, 673–685.

(18) Zhang, Y.; Shi, S.; Chen, X.; Peng, M. Functionalized Magnetic Nanoparticles Coupled with Mass Spectrometry for Screening and Identification of Cyclooxygenase-1 Inhibitors from Natural Products. *J. Chromatogr., B* **2014**, *960*, 126–132.

(19) Liang, R.-P.; Yao, G.-H.; Fan, L.-X.; Qiu, J.-D. Magnetic Fe3O4@Au Composite-Enhanced Surface Plasmon Resonance for Ultrasensitive Detection of Magnetic Nanoparticle-Enriched α-Fetoprotein. *Anal. Chim. Acta* **2012**, *737*, 22–28.

(20) Huang, S.-Y.; Chen, Y.-C. Magnetic Nanoparticle-Based Platform for Characterization of Histidine-Rich Proteins and Peptides. *Anal. Chem.* **2013**, *85*, 3347–3354.

(21) Asfaram, A.; Ghaedi, M.; Goudarzi, A.; Soylak, M.; Mehdizadeh Langroodi, S. Magnetic Nanoparticle Based Dispersive Micro-Solid-Phase Extraction for the Determination of Malachite Green in Water Samples: Optimized Experimental Design. *New J. Chem.* **2015**, *39*, 9813–9823.

(22) Bruls, D. M.; Evers, T. H.; Kahlman, J. A. H.; van Lankvelt, P. J. W.; Ovsyanko, M.; Pelssers, E. G. M.; Schleipen, J. J. H. B.; de Theije, F. K.; Verschuren, C. A.; van der Wijk, T.; van Zon, J. B. A.; Dittmer, W. U.; Immink, A. H. J.; Nieuwenhuis, J. H.; Prins, M. W. J. Rapid Integrated Biosensor for Multiplexed Immunoassays Based on Actuated Magnetic Nanoparticles. *Lab Chip* **2009**, *9*, 3504.

(23) Haun, J. B.; Yoon, T.-J.; Lee, H.; Weissleder, R. Magnetic Nanoparticle Biosensors. *Wiley Interdiscip. Rev.: Nanomed. Nanobiotechnol.* **2010**, *2*, 291–304.

(24) Chuah, K.; Wu, Y.; Vivekchand, S. R. C.; Gaus, K.; Reece, P. J.; Micolich, A. P.; Gooding, J. J. Nanopore Blockade Sensors for Ultrasensitive Detection of Proteins in Complex Biological Samples. *Nat. Commun.* **2019**, *10*, 2109.

(25) Anna, S. L.; Bontoux, N.; Stone, H. A. Formation of Dispersions Using "Flow Focusing" in Microchannels. *Appl. Phys. Lett.* **2003**, *82*, 364–366.

(26) Garstecki, P.; Fuerstman, M. J.; Stone, H. A.; Whitesides, G. M. Formation of Droplets and Bubbles in a Microfluidic T-Junction—Scaling and Mechanism of Break-Up. *Lab Chip* **2006**, *6*, 437.

(27) Shang, L.; Cheng, Y.; Zhao, Y. Emerging Droplet Microfluidics. *Chem. Rev.* **2017**, *117*, 7964–8040.

(28) Chen, Y.; Gao, W.; Zhang, C.; Zhao, Y. Three-Dimensional Splitting Microfluidics. *Lab Chip* **2016**, *16*, 1332–1339.

(29) Huebner, A.; Bratton, D.; Whyte, G.; Yang, M.; deMello, A. J.; Abell, C.; Hollfelder, F. Static Microdroplet Arrays: A Microfluidic Device for Droplet Trapping, Incubation and Release for Enzymatic and Cell-Based Assays. *Lab Chip* **2009**, *9*, 692–698.

(30) Czilwik, G.; Messinger, T.; Strohmeier, O.; Wadle, S.; von Stetten, F.; Paust, N.; Roth, G.; Zengerle, R.; Saarinen, P.; Niittymäki, J.; McAllister, K.; Sheils, O.; O'Leary, J.; Mark, D. Rapid and Fully Automated Bacterial Pathogen Detection on a Centrifugal-Micro-

https://dx.doi.org/10.1021/acsomega.0c02892
ACS Omega 2020, 5, 20609–20617

fluidic LabDisk Using Highly Sensitive Nested PCR with Integrated Sample Preparation. *Lab Chip* **2015**, *15*, 3749−3759.
(31) Boedicker, J. Q.; Li, L.; Kline, T. R.; Ismagilov, R. F. Detecting Bacteria and Determining Their Susceptibility to Antibiotics by Stochastic Confinement in Nanoliter Droplets Using Plug-Based Microfluidics. *Lab Chip* **2008**, *8*, 1265.
(32) Tang, M. Y. H.; Shum, H. C. One-Step Immunoassay of C-Reactive Protein Using Droplet Microfluidics. *Lab Chip* **2016**, *16*, 4359−4365.
(33) Han, S.-I.; Soo Kim, H.; Han, A. In-Droplet Cell Concentration Using Dielectrophoresis. *Biosens. Bioelectron.* **2017**, *97*, 41−45.
(34) Mazutis, L.; Gilbert, J.; Ung, W. L.; Weitz, D. A.; Griffiths, A. D.; Heyman, J. A. Single-Cell Analysis and Sorting Using Droplet-Based Microfluidics. *Nat. Protoc.* **2013**, *8*, 870−891.
(35) Zhu, Z.; Yang, C. J. Hydrogel Droplet Microfluidics for High-Throughput Single Molecule/Cell Analysis. *Acc. Chem. Res.* **2017**, *50*, 22−31.
(36) Svensson, C.-M.; Shvydkiv, O.; Dietrich, S.; Mahler, L.; Weber, T.; Choudhary, M.; Tovar, M.; Figge, M. T.; Roth, M. Coding of Experimental Conditions in Microfluidic Droplet Assays Using Colored Beads and Machine Learning Supported Image Analysis. *Small* **2019**, *15*, 1802384.
(37) Guetschow, E. D.; Steyer, D. J.; Kennedy, R. T. Subsecond Electrophoretic Separations from Droplet Samples for Screening of Enzyme Modulators. *Anal. Chem.* **2014**, *86*, 10373−10379.
(38) Barnes, S. E.; Cygan, Z. T.; Yates, J. K.; Beers, K. L.; Amis, E. J. Raman Spectroscopic Monitoring of Droplet Polymerization in a Microfluidic Device. *Analyst* **2006**, *131*, 1027.
(39) Schütt, J.; Ibarlucea, B.; Illing, R.; Zörgiebel, F.; Pregl, S.; Nozaki, D.; Weber, W. M.; Mikolajick, T.; Baraban, L.; Cuniberti, G. Compact Nanowire Sensors Probe Microdroplets. *Nano Lett.* **2016**, *16*, 4991−5000.
(40) Elbuken, C.; Glawdel, T.; Chan, D.; Ren, C. L. Detection of Microdroplet Size and Speed Using Capacitive Sensors. *Sens. Actuators, A* **2011**, *171*, 55−62.
(41) Nguyen, N.-T. Micro-Magnetofluidics: Interactions between Magnetism and Fluid Flow on the Microscale. *Microfluid. Nanofluid.* **2012**, *12*, 1−16.
(42) Yang, R.-J.; Hou, H.-H.; Wang, Y.-N.; Fu, L.-M. Micro-Magnetofluidics in Microfluidic Systems: A Review. *Sens. Actuators, B* **2016**, *224*, 1−15.
(43) Lin, G.; Baraban, L.; Han, L.; Karnaushenko, D.; Makarov, D.; Cuniberti, G.; Schmidt, O. G. Magnetoresistive Emulsion Analyzer. *Sci. Rep.* **2013**, *3*, 2548.
(44) Lin, G.; Makarov, D.; Medina-Sánchez, M.; Guix, M.; Baraban, L.; Cuniberti, G.; Schmidt, O. G. Magnetofluidic Platform for Multidimensional Magnetic and Optical Barcoding of Droplets. *Lab Chip* **2015**, *15*, 216−224.
(45) Karnaushenko, D.; Baraban, L.; Ye, D.; Uguz, I.; Mendes, R. G.; Rümmeli, M. H.; de Visser, J. A. G. M.; Schmidt, O. G.; Cuniberti, G.; Makarov, D. Monitoring Microbial Metabolites Using an Inductively Coupled Resonance Circuit. *Sci. Rep.* **2015**, *5*, 12878.
(46) Lin, G.; Makarov, D.; Melzer, M.; Si, W.; Yan, C.; Schmidt, O. G. A Highly Flexible and Compact Magnetoresistive Analytic Device. *Lab Chip* **2014**, *14*, 4050−4058.
(47) Lin, G.; Karnaushenko, D. D.; Bermúdez, G. S. C.; Schmidt, O. G.; Makarov, D. Magnetic Suspension Array Technology: Controlled Synthesis and Screening in Microfluidic Networks. *Small* **2016**, *12*, 4553−4562.
(48) Song, W.; Lin, G.; Ge, J.; Fassbender, J.; Makarov, D. Encoding Microreactors with Droplet Chains in Microfluidics. *ACS Sens.* **2017**, *2*, 1839−1846.
(49) Lin, G.; Makarov, D.; Schmidt, O. G. Magnetic Sensing Platform Technologies for Biomedical Applications. *Lab Chip* **2017**, *17*, 1884−1912.
(50) Ejsing, L.; Hansen, M. F.; Menon, A. K.; Ferreira, H. A.; Graham, D. L.; Freitas, P. P. Planar Hall Effect Sensor for Magnetic Micro- and Nanobead Detection. *Appl. Phys. Lett.* **2004**, *84*, 4729−4731.
(51) Kim, H.; Reddy, V.; Kim, K. W.; Jeong, I.; Hu, X. H.; Kim, C. Single Magnetic Bead Detection in a Microfluidic Chip Using Planar Hall Effect Sensor. *J. Magnetics* **2014**, *19*, 10−14.
(52) Osterberg, F. W.; Dalslet, B. T.; Damsgaard, C. D.; Freitas, S. C.; Freitas, P. P.; Hansen, M. F. Bead Capture on Magnetic Sensors in a Microfluidic System. *IEEE Sens. J.* **2009**, *9*, 682−688.
(53) Kokkinis, G.; Cardoso, S.; Keplinger, F.; Giouroudi, I. Microfluidic Platform with Integrated GMR Sensors for Quantification of Cancer Cells. *Sens. Actuators, B* **2017**, *241*, 438−445.
(54) Baselt, D. R.; Lee, G. U.; Natesan, M.; Metzger, S. W.; Sheehan, P. E.; Colton, R. J. A Biosensor Based on Magnetoresistance Technology. *Biosens. Bioelectron.* **1998**, *13*, 731−739.
(55) Quynh, L. K.; Tu, B. D.; Dang, D. X.; Viet, D. Q.; Hien, L. T.; Huong Giang, D. T.; Duc, N. H. Detection of Magnetic Nanoparticles Using Simple AMR Sensors in Wheatstone Bridge. *J. Sci.: Adv. Mater. Devices* **2016**, *1*, 98−102.
(56) Miller, M. M.; Prinz, G. A.; Cheng, S.-F.; Bounnak, S. Detection of a Micron-Sized Magnetic Sphere Using a Ring-Shaped Anisotropic Magnetoresistance-Based Sensor: A Model for a Magnetoresistance-Based Biosensor. *Appl. Phys. Lett.* **2002**, *81*, 2211−2213.
(57) Reiss, G.; Brueckl, H.; Huetten, A.; Schotter, J.; Brzeska, M.; Panhorst, M.; Sudfeld, D.; Becker, A.; Kamp, P. B.; Puehler, A.; Wojczykowski, K.; Jutzi, P. Magnetoresistive Sensors and Magnetic Nanoparticles for Biotechnology. *J. Mater. Res.* **2005**, *20*, 3294−3302.
(58) Cardoso, F. A.; Germano, J.; Ferreira, R.; Cardoso, S.; Martins, V. C.; Freitas, P. P.; Piedade, M. S.; Sousa, L. Detection of 130nm Magnetic Particles by a Portable Electronic Platform Using Spin Valve and Magnetic Tunnel Junction Sensors. *J. Appl. Phys.* **2008**, *103*, No. 07A310.
(59) Li, G.; Sun, S.; Wilson, R. J.; White, R. L.; Pourmand, N.; Wang, S. X. Spin Valve Sensors for Ultrasensitive Detection of Superparamagnetic Nanoparticles for Biological Applications. *Sens. Actuators, A* **2006**, *126*, 98−106.
(60) Jitariu, A.; Ghemes, C.; Lupu, N.; Chiriac, H. Magnetic Particles Detection by Using Spin Valve Sensors and Magnetic Traps. *AIP Adv.* **2017**, *7*, No. 056616.
(61) Dalslet, B. T.; Damsgaard, C. D.; Donolato, M.; Strømme, M.; Strömberg, M.; Svedlindh, P.; Hansen, M. F. Bead Magneto-relaxometry with an On-Chip Magnetoresistive Sensor. *Lab Chip* **2011**, *11*, 296−302.
(62) Pekas, N.; Porter, M. D.; Tondra, M.; Popple, A.; Jander, A. Giant Magnetoresistance Monitoring of Magnetic Picodroplets in an Integrated Microfluidic System. *Appl. Phys. Lett.* **2004**, *85*, 4783−4785.
(63) Maleki, M. A.; Soltani, M.; Kashaninejad, N.; Nguyen, N.-T. Effects of Magnetic Nanoparticles on Mixing in Droplet-Based Microfluidics. *Phys. Fluids* **2019**, *31*, No. 032001.
(64) Lehmann, U.; Vandevyver, C.; Parashar, V. K.; Gijs, M. A. M. Droplet-Based DNA Purification in a Magnetic Lab-on-a-Chip. *Angew. Chem., Int. Ed.* **2006**, *45*, 3062−3067.
(65) Varma, V. B.; Ray, A.; Wang, Z. M.; Wang, Z. P.; Ramanujan, R. V. Droplet Merging on a Lab-on-a-Chip Platform by Uniform Magnetic Fields. *Sci. Rep.* **2016**, *6*, 37671.
(66) Jeong, I.; Eu, Y.-J.; Kim, K. W.; Hu, X.; Sinha, B.; Kim, C. Magnetic Sensor-Based Detection of Picoliter Volumes of Magnetic Nanoparticle Droplets in a Microfluidic Chip. *Journal of Magnetics* **2012**, *17*, 302−307.
(67) Nhalil, H.; Givon, T.; Das, P. T.; Hasidim, N.; Mor, V.; Schultz, M.; Amrusi, S.; Klein, L.; Grosz, A. Planar Hall Effect Magnetometer With 5 pT Resolution. *IEEE Sens. Lett.* **2019**, *3*, 1−4.
(68) Granell, P. N.; Wang, G.; Cañon Bermudez, G. S.; Kosub, T.; Golmar, F.; Steren, L.; Fassbender, J.; Makarov, D. Highly Compliant Planar Hall Effect Sensor with Sub 200 NT Sensitivity. *npj Flex. Electron.* **2019**, *3*, 3.
(69) Melzer, M.; Karnaushenko, D.; Makarov, D.; Baraban, L.; Calvimontes, A.; Mönch, I.; Kaltofen, R.; Mei, Y.; Schmidt, O. G. Elastic Magnetic Sensor with Isotropic Sensitivity for In-Flow Detection of Magnetic Objects. *RSC Adv.* **2012**, *2*, 2284−2288.

https://dx.doi.org/10.1021/acsomega.0c02892
ACS Omega 2020, 5, 20609−20617

(70) Yadav, S.; Masud, M. K.; Islam, M. N.; Gopalan, V.; Lam, A. K.; Tanaka, S.; Nguyen, N.-T.; Hossain, M. S. A.; Li, C.; Yamauchi, M. Y.; Shiddiky, M. J. A. Gold-Loaded Nanoporous Iron Oxide Nanocubes: A Novel Dispersible Capture Agent for Tumor-Associated Autoantibody Analysis in Serum. *Nanoscale* **2017**, *9*, 8805−8814.
(71) Grosz, A.; Mor, V.; Paperno, E.; Amrusi, S.; Faivinov, I.; Schultz, M.; Klein, L. Planar Hall Effect Sensors With Subnanotesla Resolution. *IEEE Magn. Lett.* **2013**, *4*, 6500104−6500104.
(72) Tensormeter − *A new dimension of resistance measurements*http://tensormeter.eu/ (accessed Dec 2, 2019).
(73) Kosub, T.; Kopte, M.; Hühne, R.; Appel, P.; Shields, B.; Maletinsky, P.; Hübner, R.; Liedke, M. O.; Fassbender, J.; Schmidt, O. G.; Makarov, D. Purely Antiferromagnetic Magnetoelectric Random Access Memory. *Nat. Commun.* **2017**, *8*, 13985.
(74) Kosub, T.; Kopte, M.; Radu, F.; Schmidt, O. G.; Makarov, D. All-Electric Access to the Magnetic-Field-Invariant Magnetization of Antiferromagnets. *Phys. Rev. Lett.* **2015**, *115*, No. 097201.
(75) Kosub, T.; Vélez, S.; Gomez-Perez, J. M.; Hueso, L. E.; Fassbender, J.; Casanova, F.; Makarov, D. Anomalous Hall-like Transverse Magnetoresistance in Au Thin Films on $Y_3Fe_5O_{12}$. *Appl. Phys. Lett.* **2018**, *113*, 222409.

https://dx.doi.org/10.1021/acsomega.0c02892
ACS Omega 2020, 5, 20609−20617